energies

MDPI

Article

Resilient Operation Strategies for Integrated Power-Gas Systems

Behdad Faridpak [1] and Petr Musilek [1,2,*]

[1] Department of Electrical and Computer Engineering, University of Alberta, Edmonton, AB T6G 1H9, Canada; faridpak@ualberta.ca
[2] Department of Applied Cybernetics, University of Hradec Králové, 500 03 Hradec Králové, Czech Republic
* Correspondence: pmusilek@ualberta.ca

Abstract: This article presents a novel methodology for analyzing the resilience of an active distribution system (ADS) integrated with an urban gas network (UGN). It demonstrates that the secure adoption of gas turbines with optimal capacity and allocation can enhance the resilience of the ADS during high-impact, low-probability (HILP) events. A two-level tri-layer resilience problem is formulated to minimize load shedding as the resilience index during post-event outages. The challenge of unpredictability is addressed by an adaptive distributionally robust optimization strategy based on multi-cut Benders decomposition. The uncertainties of HILP events are modeled by different moment-based probability distributions. In this regard, considering the nature of each uncertain variable, a different probabilistic method is utilized. For instance, to account for the influence of power generated from renewable energy sources on the decision-making process, a diurnal version of the long-term short-term memory network is developed to forecast day-ahead weather. In comparison with standard LSTM, the proposed approach reduces the mean absolute error and root mean squared error by approximately 47% and 71% for wind speed, as well as 76% and 77% for solar irradiance network. Finally, the optimal operating framework for improving power grid resilience is validated using the IEEE 33-bus ADS and 7-node UGN.

Keywords: multi-energy system; optimal operation; resilient power system; adaptive distributionally robust optimization

Citation: Faridpak, B.; Musilek, P. Resilient Operation Strategies for Integrated Power-Gas Systems. *Energies* **2024**, *17*, 6270. https://doi.org/10.3390/en17246270

Academic Editor: Andres Siirde

Received: 24 October 2024
Revised: 3 December 2024
Accepted: 9 December 2024
Published: 12 December 2024

1. Introduction

Extreme weather conditions and man-made attacks have contributed to catastrophic power grid failures, leading to a growing global need for improvements in power system resilience. In this context, resilience refers to the ability of the power grid to meet an acceptable level of electricity demand during HILP events, where most power outages are limited to a few hours [1]. However, even short-time power outages can have significant consequences, especially when CLs are involved. Therefore, it is important to improve the resilience of ADS with economically efficient solutions for post-event load restoration.

A possible solution to improve system resilience is to connect a UGN and other local sources, such as RES, and coordinate their operation with the ADS. Compared to installing new components, using existing durable energy infrastructure is an effective approach, especially under common geographical and techno-economical limitations. The underground infrastructure is also better protected from HILP events [2]. However, the coordination of multiple energy systems for resilience enhancement is rarely considered. In addition, to the best of our knowledge, existing strategies only couple ADS and UGN on a predefined common bus. In the industrial practice of North American and European electric power utilities, ADS and UGN are usually coordinated by optimizing the location and capacity of GTs supplied with interruptible gas services [3–5]. Energy transfer is achieved through day-ahead gas-to-power contracts, which are more economical and practical than real-time contracts [6].

There are two main challenges in the area of resilience-oriented integration of multi-energy systems: (1) Modeling the intensity of the HILP events and their influence on ADS;

and (2) Optimizing the operation of ADS with weather-related power generated from RES, to determine appropriate locations and capacities of the coupling points. To address these challenges, there is a need for innovative solutions to improve the resilience of multi-energy systems and enhance the hardiness and stability of the power grid.

2. Literature Review

Optimization techniques for improving the resilience of the power grid have become a new field of research and development, with numerous studies focusing on short- and long-term improvements. Kwasinski [7] addressed the availability of power supply using a risk assessment method to improve resilience to hurricanes. Ahmed et al. [8] proposed to enhance resilience against false data injection attacks by equal power sharing in multi-area power systems. Xu et al. [9] used a stochastic integer program to minimize the average time that customers are without power. Similarly, Trakas and Hatziargyriou [10] described a stochastic programming solution to increase the resilience of the distribution system and minimize l^{sh} during a wildfire. The authors considered uncertainties associated with s, v, and the direction of the wind. According to Sharma et al. [11], distributed generators improved ADS resilience during islanding by mitigating the risks associated with uncertainties in load demand and RES generation. Wang et al. [12] studied the restoration of CLs in the presence of distributed generators and ESS using microgrid formation methods. Xu et al. [13] considered a priority for supplying CLs in demand response to enhance the resilience of distribution networks under extreme scenarios. Wang et al. [14] used an iterative algorithm considering an unbalanced three-phase power flow to develop an optimal decision-making method for serving CLs after blackouts. Robust tri-level planning for distributed energy resources was proposed by Samani and Aminifar [15] to solve the problem of enhancing resilience using column and constraint generation with BD. The use of electric vehicles as a backup power resource and their positive impact on resilience were discussed by Hussain and Musilek [16].

In addition to approaches based on locally distributed RES, the resilience of ADS can also be improved through the integration of other energy systems, decreasing the probability of load shedding. The technical and economic benefits of integrated energy systems were previously discussed by the authors [17–19]. According to [17], UGN is one of the most appropriate and readily available energy systems to integrate with ADS. There have been several studies conducted to optimize IDGS operation, including different strategies and coordination levels for coupling ADS and UGN. In general, IDGS optimization approaches can be categorized as sequential or simultaneous. In sequential optimization, the energy cost of ADS and UGN is minimized by defining two distinct objective functions. In contrast, simultaneous optimization strategies use a fully coupled IDGS operated by a single entity [20].

Due to the interdependence of multiple energy systems, a disruption in any of them can compromise the energy supply of the other ones. Ravadanegh et al. [2] modeled the effects of weather-related HILPs with various levels using multiphase performance response curves. In this way, they determined the time-dependent performance levels of the IDGS. Using the onsite supply strategy of the energy storage systems and demand response, Darvish et al. [3] enhanced the resilience of IDGS considering reserve scheduling and pre-event responses. Saravi et al. [21] introduced a resilience-oriented aggregator–agent splitting framework for IDGS. Cong et al. [22] presented a robust three-stage optimization model for the resilient operation of IDGS to minimize load curtailments imposed by attacks. Manshadi and Khodayar [23] described a bi-level optimization problem to address the optimal operation of multi-energy microgrids while considering the security and resilience of the system. Correa-Posada and Śanchez-Martın [24] presented a unique MILP approach for the power and gas flow considering security constraints for both normal and contingency scenarios. Wang et al. [25] increased IDGS resilience by protecting its most vulnerable components using tri-level MILP optimization. Sawas et al. [26] proposed

a cyberattack-resistant scheduling model using supervised and unsupervised false data detection techniques.

Due to the high penetration rate of RES in ADS and their impact on resilience, accurate weather forecasting is crucial to formulate operating strategies. This can be accomplished using data-driven algorithms that evaluate time series of meteorological data and predict the power produced by RESs. To cope with the complex behavior of the weather and related uncertainties, machine learning algorithms (such as support vector machines, linear regression, or tree-based models) have often been used for this task [27]. However, these algorithms are not easily scaled to large data sets. Shoaei et al. [28] conducted a comprehensive study on the applications of artificial intelligence in renewable energy systems. A possible solution is to implement a robust technique with multivariate mapping capabilities. To take into account the time-series nature of weather data, recurrent neural networks allow feedback connections between their hidden layers. However, their applicability is limited due to the vanishing gradient problem. This and other issues have been alleviated by LSTM neural network models which have been successfully used for weather-dependent time series [29]. For example, Abdel-Nasser et al. [30] used LSTM to predict solar irradiation from input data aggregated by combining the Choquet integral using a fuzzy measure. Wang et al. [31] implemented an LSTM with a novel least absolute shrinkage and selection operator to increase the accuracy of short-term predictions. Zhou et al. [32] proposed a technique to improve the accuracy of LSTM by extracting significant features from the input. Two-dimensional convolutional neural networks and bidirectional LSTM units were used to predict wind power by Dolatabadi et al. [33]. In addition, Li et al. [34] used mathematical morphology to improve the accuracy of LSTM for wind speed forecasts.

This article deals with the optimal operation of ADS. The main objective is to improve the resilience of the electricity grid by coupling it with the UGN through GTs. To determine the capacities and locations of the GTs, we formulate a two-level tri-layer resilience-oriented optimal operation problem. Due to the unknown post-event status of the system, the problem is solved by a set of distribution functions. As a result, the uncertain consequences of HILP events are modeled by a probabilistic framework solved by an ADRO approach.

The required capacity of GTs depends on load specifications and generation from local RESs, influenced by extreme weather conditions. Therefore, to model these uncertainties, we construct moment-based probability distributions. Furthermore, by considering historical weather data, we propose an enhanced forecasting method based on a modified LSTM algorithm to predict expected weather-dependent RES generation.

To provide proper context, existing studies are compared in Table 1 along with the approach described in this article. Previous studies have addressed resilience in power systems using various optimization methods such as MINLP [1] and MILP [2]. Nevertheless, these methods cannot effectively handle the complex and uncertain nature of HILP events when RESs are involved. Although probabilistic approaches such as ARO [35] and RO [36] have been employed for uncertainty modeling, they lack the ability to address ambiguity sets created by more advanced uncertainty handling methods. In contrast, the proposed approach utilizes ADRO in combination with ambiguity sets, offering a more robust framework to handle both proactive and restoration processes. In addition, the solution methodology requires an efficient approach to capture these complexities. For instance, approaches like stochastic [10] and relaxation [12] methods are not efficient due to their high computational cost and inability to properly incorporate the impact of uncertainties. The proposed MCBD method provides a cost-effective and scalable solution to overcome IDGS resilience improvement challenges.

The major contributions are as follows.

1. A new approach to enhancing the resilience of ADS with the following properties:
   (a) A novel formulation of the resilience enhancement problem: Distribution functions of random post-event consequences are used in the calculations to address the probabilistic status of ADS. The performance of the proposed

model is evaluated by extensive comparative simulations considering different levels of robustness and resilience indices.

(b) A modified multi-cut decomposition method: To analyze the various effects of each probabilistic consequence and to address the complexity of the problem, a modified version of the decomposition approach is implemented. The multi-cut decomposition method captures more detailed information about the system, which is critical for managing the random post-event status of HILP events.

(c) Optimal use of the potential of existing natural gas infrastructure: The proposed approach determines the most resilient, secure and cost-efficient coordination points between ADS and UGN.

2. A new momentum-based approach with the following properties:

(a) A learning-based approach to calculate the statistics of momentum: Training does not require complex filtering or pre-processing methods. The data presentation is modified to ensure smooth domain variation, transforming the prediction method from an hourly domain into a diurnal domain, and executing hourly predictive subtasks in parallel to construct probability distributions.

(b) Improved accuracy in comparison with conventional LSTM network: The proposed diurnal learning approach is validated using multiple accuracy indicators and compared with the conventional approach.

Table 1. Comparative analysis of resilience-oriented methods.

Ref.	Optimization Method	Solution Method	Enhancement Method	Process Time		Uncertainty Handling	RSC	IDGS
				Proactive	Restoration			
[1]	MINLP	-	RES	✓	-	-	-	-
[2]	MILP	-	EH	-	✓	-	-	✓
[36]	MILP	RO	GT	-	✓	US	-	✓
[6]	MILP	NC&CG	GT	✓	✓	RBN		✓
[10]	MINLP	Stochastic	Hardening	-	✓	MC	-	-
[12]	MISDP	Relaxation	ES and DG	-	✓	-	-	-
[26]	-	Classification	BI	-	✓	NN	-	✓
[35]	ARO	C&CG	EH	✓	-	TI		-
[37]	RO	BD and C&CG	EH	-	✓	US		-
[38]	MINLP	MCB	-	-	✓	-	-	-
Proposed	ADRO	MCBD	GT	✓	✓	AS	✓	✓

MISDP: Mixed-integer semi-definite programming, NC&CG: nested column and constraint generation, MCB: modified combinatorial Benders, EH: emergency handling, DG: distributed generation, RBN: randomized binary numbers, BI: bidirectional interconnection, TI: three intervals, US: uncertainty set, NN: neural network, AS: ambiguity set, RSC: resilient and secure coordination.

3. Problem Formulation

To analyze the resilience enhancement of the ADS, two phases of system operation are defined: the pre-event and post-event, denoted by superscripts of 0 and 1, respectively. The main assumptions of the proposed approach are:

- The load is considered event-independent. In other words, the load is the same pre-event and post-event. However, since the specifications of an extreme event are unpredictable, the necessity of load supply (i.e., criticality of the load, CL/NCL) is randomly changed in the post-event phase.

- Towers and lines of the analyzed system are assumed to have similar fragility functions. Their restoration time is greater than the total optimization time interval T.
- Optimal AC power flow is used as a dispatch tool, assuming a reactive power balance among buses.
- After a HILP event, damage on the supply side and isolation from different zones and/or upstream power grid force reliance on local sources, such as RESs and ESSs.
- Interruption of any power source causes load shedding; the coordination with the UGN through GTs provides improved resilience against load shedding in the ADS.

3.1. Pre-Event

Under normal operation, without any faults in the system, the primary objective is to supply the load with the minimum power consumption.

$$\underset{P^{\mathrm{P}}}{\mathrm{Min}} \sum_{t=1}^{T} C_t^{\mathrm{P}} P_t^{\mathrm{P},0}, \tag{1}$$

where C^{P} is the power price, P^{P} and Q^{P} are the active and reactive power received from the upstream grid, respectively, T is the total operation time, and D is the total number of days in the data set. Symbols K, N, C, and Z express, respectively, the total number of buses, nodes, coordination points, and zones. Superscript $(.)^{0/1}$ is used to indicate pre-/post-event notation, and subscript t is the time index.

The objective function (1) is subject to the following constraints:

$$P_t^{\mathrm{P},0} + P_{k,t}^{\mathrm{WT}} + P_{k,t}^{\mathrm{PV}} + P_{k,t}^{\mathrm{dch},0} = \sum_{k,j}^{B} P_{kj,t}^{0} + r_{kj} I_{kj,t}^{0} + P_{k,t}^{\mathrm{L}} + P_{k,t}^{\mathrm{ch},0} \qquad \forall t, \forall k \tag{2}$$

$$Q_t^{\mathrm{P},0} + Q_{k,t}^{\mathrm{WT}} = \sum_{k,j}^{B} Q_{kj,t}^{0} + x_{kj} I_{kj,t}^{0} + Q_{k,t}^{\mathrm{L}} \qquad \forall t, \forall k \tag{3}$$

$$(P_{kj,t}^{0})^2 + (Q_{kj,t}^{0})^2 \leq I_{kj,t}^{0} U_{k,t}^{0} \qquad \forall t, \forall k \tag{4}$$

$$U_{k,t}^{0} - U_{j,t}^{0} = 2P_{kj,t}^{0} r_{ij} + 2Q_{kj,t}^{0} x_{ij} - I_{kj,t}^{0} \left(r_{kj}^2 + x_{kj}^2 \right) \qquad \forall t, \forall k \tag{5}$$

$$P^{\mathrm{P,min}} \leq P_t^{\mathrm{P},0} \leq P^{\mathrm{P,max}} \qquad \forall t \tag{6}$$

$$Q^{\mathrm{P,min}} \leq Q_t^{\mathrm{P},0} \leq Q^{\mathrm{P,max}} \qquad \forall t \tag{7}$$

$$U_k^{\min} \leq U_{k,t}^{0} \leq U_k^{\max} \qquad \forall t, \forall k \tag{8}$$

$$0 \leq I_{kj,t}^{0} \leq I_{kj}^{\max} \qquad \forall t, \forall k \tag{9}$$

where P^{WT}, Q^{WT}, and $/P^{PV}$ are the amounts of power generated from RESs, P^{L} and Q^{L} are active and reactive load demands, and P^{ch} and P^{dch} are the charging and discharging powers of ESS, respectively. Symbols r and x mark resistance and inductance, while I and U represent the squared magnitudes of current and voltage, respectively. The superscripts $(.)^{\max}$ and $(.)^{\min}$ are the maximum and minimum limitations.

Equations (2) and (3) describe the constraints on the active and reactive power, respectively. They state that the amounts of power generated by different suppliers must be balanced with the amounts consumed. Branch flow is calculated using (4) and (5). Finally, the constraints on the active and reactive power, voltage and current received from the upstream grid are specified in (6)–(9).

The power generated from the RESs is formulated as follows [19].

$$P_{t,k}^{\mathrm{WT}} = \begin{cases} 0, & 0 \le v_t \le v_{\mathrm{ci}} \text{ or } v_t \ge v_{\mathrm{co}} \\ \frac{P_k^{\mathrm{WT,max}}(v_t - v_{\mathrm{ci}})}{(v_{\mathrm{r}} - v_{\mathrm{ci}})}, & v_{\mathrm{ci}} \le v_t \le v_{\mathrm{r}} \\ P_k^{\mathrm{WT,max}}, & v_r \le v_t \le v_{co} \end{cases} \quad \forall t, \forall k \tag{10}$$

$$0 \le P_{t,k}^{\mathrm{WT}} \le P_k^{\mathrm{WT,max}} \quad \forall t, \forall k \tag{11}$$

$$P_{t,k}^{\mathrm{PV}} = \begin{cases} \frac{P_k^{\mathrm{PV,max}} \times s_t}{s_{\mathrm{r}}}, & 0 \le s_t \le s_{\mathrm{r}} \\ P_k^{\mathrm{PV,max}}, & s_{\mathrm{r}} \le s_t \end{cases} \quad \forall t, \forall k \tag{12}$$

$$0 \le P_{t,k}^{\mathrm{PV}} \le P_k^{\mathrm{PV,max}} \quad \forall t, \forall k, \tag{13}$$

where parameters v_{ci}, v_{co}, and v_r are cut-in, cut-out, and rated wind speed. Additionally, the rated solar radiation, solar radiation, and wind speed are shown by s_r, s, and v, respectively.

ESSs are commonly used to mitigate the unpredictable nature of nondispatchable, intermittent RESs. The technical operating constraints of ESSs can be modeled as follows.

$$E_{k,t+1}^0 = E_{k,t}^0 + [P_{k,t}^{\mathrm{ch},0}.\eta - P_{k,t}^{\mathrm{dch},0}/\eta].\Delta t \quad \forall t, \forall k \tag{14}$$

$$0 \le P_{k,t}^{\mathrm{ch},0} \le I_{k,t}^{\mathrm{ch},0}.P_k^{\mathrm{ch,max}} \quad \forall t, \forall k, I_{k,t}^{\mathrm{ch},0} \in \{0,1\} \tag{15}$$

$$0 \le P_{k,t}^{\mathrm{dch},0} \le (1 - I_{k,t}^{\mathrm{ch},0}).P_k^{\mathrm{dch,max}}.\beta \quad \forall t, \forall k, I_{k,t}^{\mathrm{ch},0} \in \{0,1\} \tag{16}$$

$$E^{\min} \le E_{k,t}^0 \le E^{\max} \quad \forall t, \forall k \tag{17}$$

$$E_{t=0}^0 = E_{t=T}^0 \quad \forall t, \forall k \tag{18}$$

E and η are state of energy and efficiency. Also, I^{ch} and I^{dch} are the charging and discharging status of ESSs, respectively.

The state of energy at time $t+1$ depends on the state of energy and the charging/discharging rate of the ESS at the previous time slot (14). The constraints of ESS include charging (15) and discharging (16) rates, state of energy limitation (17), and the requirement of equality between the initial and final state of energy (18).

3.2. Post-Event

An extreme event, such as a weather-related disaster, can cause interruptions on the supply side. As a result, the electric load cannot be served efficiently. In most cases, locally distributed generators (such as PV, WT, and ESS) cannot entirely meet the load demands. The use of other available energy infrastructure, such as the UGN, is a possible approach to solve the problem of inadequate power supply. For example, power sources, including the upstream power grid or RESs, may be interrupted after a HILP event. In such cases, to avoid load shedding and substitute power shortage, GTs should be allocated to appropriate buses. Coordination between the ADS and the UGN can provide an effective approach to improve resilience.

Assuming C secure coordination points, the following objective function can be defined using natural gas price C^G, natural gas consumed by GTs G^{GT}, and penalty of load shedding ρ. The goal is to minimize the operational costs of the IDGS

$$\underset{\substack{P^{\mathrm{P}}, G^{\mathrm{GT}}, \\ l^{\mathrm{sh}}}}{\mathrm{Min}} \sum_{t=1}^{T} \left\{ C_t^{\mathrm{P}} P_t^{\mathrm{P},1} + \sum_{c=1}^{C} C_t^{\mathrm{G}} G_{t,c}^{\mathrm{GT},1} + \sum_{k=1}^{K} \rho l_{t,k}^{\mathrm{sh},1} \right\}, \tag{19}$$

subject to the following constraints

$$P_t^{\mathrm{P},1} + P_{k,t}^{\mathrm{WT}} + P_{k,t}^{\mathrm{PV}} + P_{k,t}^{\mathrm{dch},1} + l_{k,t}^{\mathrm{sh},1} = \sum_{k,j}^{B} P_{kj,t}^{1} + r_{kj} I_{kj,t}^{1} + P_{k,t}^{\mathrm{L}} + P_{k,t}^{\mathrm{ch},1} \qquad \forall t, \forall k \tag{20}$$

$$Q_t^{\mathrm{P},1} + Q_{k,t}^{\mathrm{WT}} = \sum_{k,j}^{B} Q_{kj,t}^{1} + x_{kj} I_{kj,t}^{1} + Q_{k,t}^{\mathrm{L}} \qquad \forall t, \forall k \tag{21}$$

$$(P_{kj,t}^{1})^2 + (Q_{kj,t}^{1})^2 \leq I_{kj,t}^{1} U_{k,t}^{1} \qquad \forall t, \forall k \tag{22}$$

$$U_{k,t}^{1} - U_{j,t}^{1} = \quad 2P_{kj,t}^{1} r_{ij} + 2Q_{kj,t}^{1} x_{ij} - I_{kj,t}^{1}\left(r_{kj}^{2} + x_{kj}^{2}\right) \qquad \forall t, \forall k \tag{23}$$

$$P^{\mathrm{P,min}} \leq P_t^{\mathrm{P},1} \leq P^{\mathrm{P,max}} \qquad \forall t \tag{24}$$

$$Q^{\mathrm{P,min}} \leq Q_t^{\mathrm{P},1} \leq Q^{\mathrm{P,max}} \qquad \forall t \tag{25}$$

$$U_k^{\min} \leq U_{k,t}^{1} \leq U_k^{\max} \qquad \forall t, \forall k \tag{26}$$

$$0 \leq I_{kj,t}^{1} \leq I_{kj}^{\max} \qquad \forall t, \forall k \tag{27}$$

$$0 \leq l_{k,t}^{\mathrm{sh},1} \leq P_{k,t}^{L} \qquad \forall t, \forall k \tag{28}$$

$$E_{k,t+1}^{1} = E_{k,t}^{1} + [P_{k,t}^{\mathrm{ch},1}.\eta - P_{k,t}^{\mathrm{dch},1}/\eta] \qquad \forall t, \forall k \tag{29}$$

$$0 \leq P_{k,t}^{\mathrm{ch},1} \leq I_{k,t}^{\mathrm{ch},1}.P_k^{\mathrm{ch,max}} \qquad \forall t, \forall k, I_{k,t}^{\mathrm{ch},1} \in \{0,1\} \tag{30}$$

$$0 \leq P_{k,t}^{\mathrm{dch},1} \leq (1 - I_{k,t}^{\mathrm{ch},1}).P_k^{\mathrm{dch,max}}.\beta \qquad \forall t, \forall k, I_{k,t}^{\mathrm{ch},1} \in \{0,1\} \tag{31}$$

$$E^{\min} \leq E_{k,t}^{1} \leq E^{\max} \qquad \forall t, \forall k \tag{32}$$

$$E_{t=0}^{1} = E_{t=T}^{1} \qquad \forall t, \forall k \tag{33}$$

where β is depth of discharge

Note that constraints (20)–(33) are similar to the formulations introduced in the previous subsection; however, load shedding is incorporated in the post-event model (20) as a resilience index.

4. Resilience-Oriented Model

HILP incidents can result in supply-side disruptions that cause load loss l_t^{sh}. Coordination among multiple sources of energy can be used to enhance the resilience of the system [14]. The proposed model addresses the optimal operational-planning strategy that coordinates multiple energy sources, including the ADS and UGN, to minimize l_t^{sh}. First, the model incorporates the uncertainty of HILP events to capture potential damage. Then, it optimizes the operation of the ADS. Finally, it plans the optimal capacity and location for coordination. In addition to enhancing resilience during HILP events, this coordination process allocates limited GT resources to supply critical loads for longer periods and improves the handling of RES uncertainties.

For the system considered in this contribution, the resilience of the ADS can be enhanced by adding GTs to appropriate buses, as a backup. Since ADS has the priority to supply CLs, their configuration, location, and ratio in the post-event situation must be modeled. The optimal resilience-oriented operation problem can be mathematically formulated using a tri-layer two-level approach. Level 1 includes determining the maximum value of l_t^{sh} as the worst-case (Layer 1) and identifying the best coordination points (Layer 2). Layer 3 then checks the security validation of the IDGS plan in the Level 2 process. Details of the proposed model are described in the following subsections.

This multi-layer, multi-stage approach requires significant computational resources, particularly when dealing with large-scale systems or highly uncertain HILP events. Nonetheless, this complexity is unavoidable to capture the full extent of uncertainties and to enhance the resilience of the system in a realistic manner. While this may pose practical challenges, especially for systems with limited computational capabilities, modern

computational tools coupled with parallel processing techniques can efficiently manage the computational load.

4.1. Level 1: Operation

The complex optimization problem at Level 1 of the proposed model is divided into two layers: Layer 1 and Layer 2. In Layer 1, various scenarios are defined. The combination of these scenarios generate multiple probability distributions. Then, the values of l_t^{sh} is calculated for the generated probability distributions. Finally, the maximum expected and feasible value of l_t^{sh} is found among all probability distributions and designated as the worst consequence for the resilience of the system.

To differentiate between CLs and NCLs, a penalty factor ρ is implemented with a different value for the two types of load such that $\rho^{\mathrm{cl}} \gg \rho^{\mathrm{ncl}}$. Hence, the last term of (19) can be reformulated by replacing the scenario-based penalty of load shedding

$$\underset{P^{\mathrm{P}},G^{\mathrm{GT}},l^{\mathrm{sh}}}{Min} \sum_{t=1}^{T} \left\{ C_t^{\mathrm{P}} P_t^{\mathrm{P},1} + \sum_{c=1}^{C} C_t^{\mathrm{G}} G_{t,c}^{\mathrm{GT},1} + \sum_{k=1}^{B} \sum_{\omega=1}^{W} \pi_\omega (\rho^{\mathrm{cl}} l_{t,k,\omega}^{\mathrm{sh|cl}} + \rho^{\mathrm{ncl}} l_{t,k,\omega}^{\mathrm{sh|ncl}}) \right\}. \tag{34}$$

where $l^{\mathrm{sh|cl}}$ and $l^{\mathrm{sh|ncl}}$ are load shedding of critical and non-critical loads.

4.2. Level 2: Secure Integration

The Level 2 equations correspond to the security check of the IDGS coordination points. To avoid the secure operational challenges of the UGN, associated with the interconnection of ADS and GTs, the following constraints of the gas system must be satisfied:

$$\bar{q}_{mn,t}^2 = C_{mn}^2 \left(p_{m,t}^2 - p_{n,t}^2 \right) \qquad \forall t, \forall m, \tag{35}$$

$$\bar{q}_{mn,t} = (q_{mn,t} - q_{nm,t})/2 \qquad \forall t, \forall m, \tag{36}$$

$$p_{mn}^{\min} \le p_{mn,t} \le p_{mn}^{\max} \qquad \forall t, \forall m, \tag{37}$$

$$LP_{mn,t} = (q_{mn,t} + q_{nm,t})\Delta t + LP_{mn,t-1} \qquad \forall t, \forall m, \tag{38}$$

$$\sum_{m,n}^{N} LP_{mn,t=0} = \sum_{m,n}^{N} LP_{mn,t=T} \ge LP^{\min} \qquad \forall t, \forall m, \tag{39}$$

$$P_{k,t}^{\mathrm{GT}} = \alpha G_{m,t}^{\mathrm{GT}} \qquad \forall t, \forall m, \tag{40}$$

$$P_k^{GT,\min} \le P_{k,t}^{\mathrm{GT}} \le P_k^{GT,\max} \qquad \forall t, \forall m, \tag{41}$$

$$P_{m,t}^{\mathrm{GT}} - RD_m^{\mathrm{GT}} \le P_{m,t+\Delta t}^{\mathrm{GT}} \le P_{m,t}^{\mathrm{GT}} + RU_m^{\mathrm{GT}} \qquad \forall t, \forall m, \tag{42}$$

where C_{mn}, p_{mn}, and LP are the Waymouth constant, node pressure of the natural gas network, and line-pack between nodes, respectively. In addition, α, $\tilde{q}(t)$, and $q_{mn,t}$ are gas-to-power conversion factor, average gas flow, and transmitted gas flow in a pipeline, respectively. Furthermore, RU^{GT} and RD^{GT} are the ramp-up and ramp-down rates of GT, respectively.

Formula (35) is the Weymouth equation of gas flow, expression (36) calculates the average value of gas transmitted through pipelines, and the nodal pressure and line-pack limits are described by (37)–(39). The GTs must be allocated at the coordination points considering the constraints (40)–(42).

For the proposed IDGS, the ADS Level 1 power balance (20) is modified as follows.

$$P_t^{\mathrm{P},1} + P_{k,t}^{\mathrm{GT}} + P_{k,t}^{\mathrm{WT}} + P_{k,t}^{\mathrm{PV}} + P_{k,t}^{\mathrm{ch},1} + l_{k,t}^{\mathrm{sh},1} = \sum_{k,j}^{B} P_{kj,t}^{1} + r_{kj} I_{kj,t}^{1} + P_{k,t}^{\mathrm{L}} + P_{k,t}^{\mathrm{dch},1} \quad \forall t, \forall k. \tag{43}$$

5. Handling of Uncertainties

The uncertainty challenges of the proposed scheduling problem are related to factors that have a substantial impact on scheduling decisions, but cannot be controlled by the sys-

tem operator. There are two major sources of uncertainty considered: the power generated by the RESs and the load specifications.

5.1. Load Specifications and Extreme Events

Although historical data on load allocation in real-world scenarios exist, the accuracy of this data may be compromised by various factors, including missing or unavailable data, high costs associated with data acquisition, and other sources of uncertainty. To address these issues, we utilize a moment-based ambiguity set for **EC** .

First, to generate multiple realization scenarios of load types at each bus, the randomly variable elements of the **EC** matrix in (44) are created using a Monte-Carlo approach [10].

$$\mathbf{EC} = \overbrace{\left.\begin{pmatrix} \mathrm{EC}_{11} & \cdots & \mathrm{EC}_{1W_1} \\ \vdots & \ddots & \vdots \\ \mathrm{EC}_{K1} & \cdots & \mathrm{EC}_{KW_1} \end{pmatrix}\right\}K}^{W_1} \quad \forall \omega_1, \forall k, \mathrm{EC}_{k,\omega_1} \in \mathcal{S}_{\mathbf{1}} \tag{44}$$

where W_1 and ω_1 are the total scenario number and sample scenarios of EC.

The elements of **EC** are factors corresponding to the CL rate that have supplying priority at bus k for scenario ω_1, and $\mathcal{S}_{\mathbf{1}} \subseteq [0,1]^{\omega_1 \times k}$ is a convex support set. For instance, if IC_{k,ω_1} is x, then x% of P_k^L is CL, while the remaining $(1-x)$% is NCL.

Second, the moment information of the uncertain variable **EC** can be defined based on the mean and covariance as follows

$$\begin{aligned} &\mathbf{EC}_{\mathcal{M}}\left(\mathcal{S}_{\mathbf{1}}, \mu_1, \mathbf{\Sigma_1}, \varsigma_1^1, \varsigma_1^2\right) = \\ &\left\{ \begin{array}{l|l} \sum\limits_{\omega_{\mathrm{p1}}=1}^{W} \pi_{\omega_{\mathrm{p1}}} = 1 & \\ \omega_{\mathrm{p1}} & \left(\mathbb{E}_{\omega_{\mathrm{p1}}}[\mathrm{EC}_{k,\omega_1}] - \mu_1\right)^T \mathbf{\Sigma_1}^{-1} \left(\mathbb{E}_{\omega_{\mathrm{p1}}}[\mathrm{EC}_{k,\omega_1}] - \mu_1\right) \le \varsigma_1^1 \\ & \mathbb{E}_{\omega_{\mathrm{p1}}}\left[(\mathrm{EC}_{k,\omega_1} - \mu_1)(\mathrm{EC}_{k,\omega_1} - \mu_1)^T \le \varsigma_1^2 \mathbf{\Sigma_1}\right] \end{array} \right\} \\ &\forall \mathrm{EC}_{k,\omega_1} \in \mathcal{S}_{\mathbf{1}}, \forall k \end{aligned} \tag{45}$$

where the probability factor and momentum-based ambiguity set are represented by π and $\mathcal{M}$, respectively. The ambiguity set $\mathbf{EC}_{\mathcal{M}}$ represents a range of possible distributions, and the optimization problem is formulated to be robust against the worst-case distribution within this set. For each bus, the total probability of distribution functions is one (45). Moreover, the mean of any distribution should be within an ellipsoidal distance limited by ς_1, and the covariance matrix should be contained within a positive semi-definite cone restricted by $\varsigma_2 \mathbf{\Sigma}$. The calculations of parameters μ, $\mathbf{\Sigma}$, ς_1, and ς_2 are expressed in (46)–(51) using the results of [39,40].

$$\mu_1 = \frac{1}{\omega_1} \sum_{\omega_1=1}^{W_1} \mathrm{EC}_{k,\omega_1} \quad \forall \mathrm{EC}_{k,\omega_1} \in \mathcal{S}_{\mathbf{1}}, \forall k \tag{46}$$

$$\mathbf{\Sigma_1} = \frac{1}{\omega_1} \sum_{\omega_1=1}^{W_1} \left(\mathrm{EC}_{k,\omega_1} - \mu_1\right)\left(\mathrm{EC}_{k,\omega_1} - \mu_1\right)^T \quad \forall \mathrm{EC}_{k,\omega_1} \in \mathcal{S}_{\mathbf{1}}, \forall k \tag{47}$$

$$\varsigma_1^1 = A_1 \tag{48}$$

$$\varsigma_1^2 = 1 + A_1 \tag{49}$$

$$A_1 = \frac{B_1^2}{\omega_1} \frac{\left(2+\sqrt{2ln\left(\frac{4}{1-\sqrt{1-\kappa}}\right)}\right)^2}{1-\frac{B_1^2}{\sqrt{\omega_1}}\left(\sqrt{1-\frac{\omega_1}{B_1^4}}+\sqrt{ln\left(\frac{4}{1-\sqrt{1-\kappa}}\right)}\right)-\left(\frac{B_1^2}{\omega_1}\right)\left(2+\sqrt{2ln\left(\frac{4}{1-\sqrt{1-\kappa}}\right)}\right)^2} \quad (50)$$

$$B_1 = \underset{\mathrm{EC}_{k,\omega_1}}{\mathrm{Max}} \left\| \frac{1}{\left(\mathrm{EC}_{k,\omega_1}-\mu_1\right)} \right\|_2 \quad (51)$$

The mean and covariance matrix of randomly generated arrays of **EC** are calculated in Equations (46) and (47), respectively. Controller parameters, $\varsigma_1 \geq 0$ in (48) and $\varsigma_2 \geq 1$ in (49) depend on the generated data to specify the size of the ambiguity set and the conservatism of optimal solutions. The auxiliary parameter A, introduced to simplify the equation, is presented in Equation (50), where κ represents the confidence level of uncertainty. Furthermore, the auxiliary variable B (51) denotes a radius region of $\mathcal{S}\mathbf{1}$ that includes EC_{k,ω_1}; here, $\|.\|_2$ indicates the second norm.

5.2. Renewable Energies and Extreme Events

To model renewable energies, the matrix **ER** is defined in (52). Based on historical data, the values in the arrays ER_{k,ω_2} can vary within an interval of 0 to the maximum power generated from RESs for each bus. Therefore, the convex support set of **ER** can be defined as $\mathcal{S}_\mathbf{2} \subseteq [0, (P_k^{\mathrm{WT,max}} + P_k^{\mathrm{PV,max}})]^{\omega_2 \times k}$.

$$\mathbf{ER} = \overbrace{\left.\begin{pmatrix} ER_{11} & \cdots & ER_{1W_2} \\ \vdots & \ddots & \vdots \\ ER_{K1} & \cdots & ER_{KW_2} \end{pmatrix}\right\}}^{W_2} K \quad \forall \omega_2, \forall k, \mathrm{ER}_{k,\omega_2} \in \mathcal{S}_\mathbf{2} \quad (52)$$

where W_2 and ω_2 are the total scenario number and sample scenarios of ER.

Similar to the **EC**, the ambiguity set $\mathbf{ER}_\mathcal{M}$ can be modeled by (53).

$$\mathbf{ER}_\mathcal{M}\left(\mathcal{S}_\mathbf{2}, \mu_2, \mathbf{\Sigma_2}, \varsigma_2^1, \varsigma_2^2\right) = \left\{ \omega_{\mathrm{p2}} \left| \begin{array}{l} \sum_{\omega_{\mathrm{p2}}=1}^{W} \pi_{\omega_{\mathrm{p2}}} = 1 \\ \left(\mathbb{E}_{\omega_{\mathrm{p2}}}[\mathrm{ER}_{k,\omega_2}] - \mu_2\right)^T \mathbf{\Sigma_2}^{-1} \left(\mathbb{E}_{\omega_{\mathrm{p2}}}[\mathrm{ER}_{k,\omega_2}] - \mu_2\right) \leq \varsigma_2^2 \\ \mathbb{E}_{\omega_{\mathrm{p2}}}\left[(\mathrm{ER}_{k,\omega_2} - \mu_2)(\mathrm{ER}_{k,\omega_2} - \mu_2)^T \leq \varsigma_2^2 \mathbf{\Sigma_2}\right] \end{array} \right. \right\}$$

$$\forall \mathrm{ER}_{k,\omega_2} \in \mathcal{S}_\mathbf{2}, \forall k \quad (53)$$

To compute the mean μ_2, we use historical data to account for the uncertainty in the RES output power. The power generation from WTs and PVs is influenced by the weather conditions, which are represented by the time series of v and s, respectively. We use the compact notation $\mathbf{u}$ to denote the real datasets of v and s. Using these real-world datasets, we aim to accurately forecast the value of μ_2.

Several studies have used deep learning methods for time-series forecasting. LSTM, in particular, has shown great promise due to its advanced units and network topology [41]. LSTM's memory units enable it to capture time-series correlations and grasp the long-term behavior of underlying systems. In this study, we use an LSTM-based forecasting approach that leverages diurnal model to calculate the values of μ_2. This approach is described in more detail below.

The conventional use of LSTM from Figure 1a is modified as shown in Figure 1b. This allows us to capture rare events and increase the overall accuracy of the model. Since pattern recognition at each time interval t is assessed on a daily basis, this modified version of the network is qualified as diurnal and named DLSTM. Considering uncertain variable $u_{t,d}$, a daily prediction approach is used instead of solving the hourly time series prediction

problem. Thus, the vertical analyses of time-series data can be transformed into a matrix-based prediction with T rows and D columns corresponding to time intervals t and days d, respectively. As shown in Figure 1b, the estimated data for each row with the same time slot t are collected as the DA forecast data $\bar{u}_{t,D+1}$.

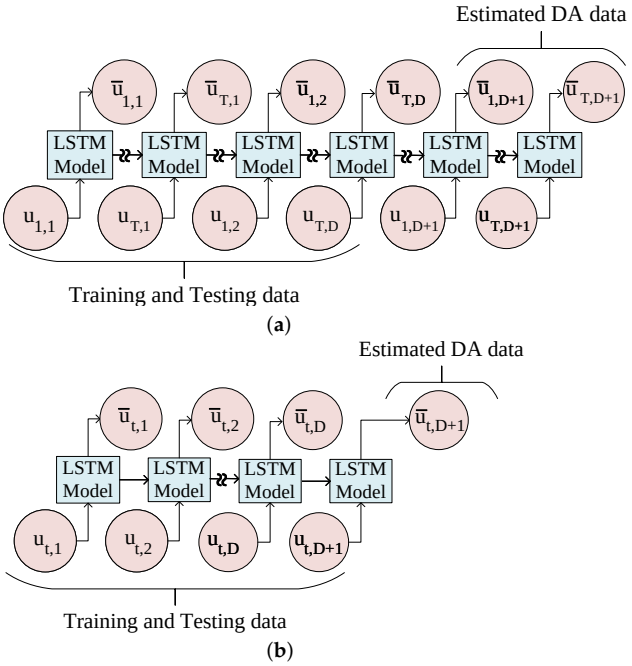

Figure 1. Implementation of the LSTM. (**a**) Conventional approach. (**b**) Proposed DLSTM approach.

The operation of the DLSTM model can be illustrated as follows: the variable v is random and non-stationary; the high randomness and fast variation of wind speed make it difficult to estimate wind speed data directly using the conventional method shown in Figure 1a. As shown in Figure 1b, a pre-processing model based on the DLSTM splits the entire data set into several time intervals for each day. This allows more effective forecasting and mitigation of the adverse effects of the stochasticity of v and s.

As shown in Figure 2, the cell sends and receives information at random intervals and the gates f_1, f_2, f_3 and f_4 follow the data flow from the cell's input to output. Furthermore, a DLSTM network's nodal formulations considering the sigmoid (σ) and the hyperbolic tangent (tanh) as activation functions are shown in [42].

$$\mathrm{f}_1 = \sigma(\mathrm{w}_1[h_{t,d-1}, u_t] + \mathrm{b}_1) \tag{54}$$
$$\mathrm{f}_2 = \sigma(\mathrm{w}_2[h_{t,d-1}, u_t] + \mathrm{b}_2) \tag{55}$$
$$\mathrm{f}_3 = \tanh(\mathrm{w}_3[h_{t,d-1}, u_t] + \mathrm{b}_3) \tag{56}$$
$$\mathrm{f}_4 = \sigma(\mathrm{w}_4[h_{t,d-1}, u_t] + \mathrm{b}_4) \tag{57}$$
$$\mathrm{f}_{t,d} = \mathrm{f}_1 \times \mathrm{f}_{t,d-1} + \mathrm{f}_2 \times \mathrm{f}_3 \tag{58}$$
$$h_{t,d} = \mathrm{f}_4 \tanh(\mathrm{f}_{t,d}) \tag{59}$$

Training the historical data using the DLSTM structure, as illustrated in Figure 1 and based on the cells depicted in Figure 2, yields deterministic DA forecasts for each time slot. However, in the context of extreme weather conditions during a HILP event, these forecasted values are designated as μ_2.

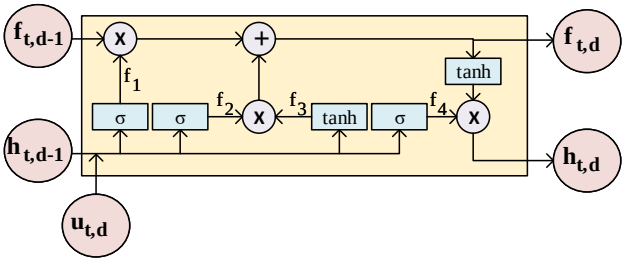

Figure 2. The structure of a DLSTM model.

The calculations of parameters $\mathbf{EC}_{\mathcal{M}}$ in (47)–(51) are rewritten for $\mathbf{ER}_{\mathcal{M}}$ in (60)–(64).

$$\mathbf{\Sigma_2} = \frac{1}{\omega_2} \sum_{\omega_1=1}^{W_1} \left(\mathrm{ER}_{k,\omega_2} - \mu_2\right)\left(\mathrm{ER}_{k,\omega_2} - \mu_2\right)^T \quad \forall \mathrm{ER}_{k,\omega_2} \in \mathcal{S}_2, \forall k \tag{60}$$

$$\varsigma_2^1 = A_2 \tag{61}$$

$$\varsigma_2^2 = 1 + A_2 \tag{62}$$

$$A_2 = \frac{B_2^2}{\omega_2} \frac{\left(2 + \sqrt{2ln\left(\frac{4}{1-\sqrt{1-\kappa}}\right)}\right)^2}{1 - \frac{B_2^2}{\sqrt{\omega_2}}\left(\sqrt{1 - \frac{\omega_2}{B_2^4}} + \sqrt{ln\left(\frac{4}{1-\sqrt{1-\kappa}}\right)}\right) - \left(\frac{B_2^2}{\omega_2}\right)\left(2 + \sqrt{2ln\left(\frac{4}{1-\sqrt{1-\kappa}}\right)}\right)^2} \tag{63}$$

$$B_2 = \underset{\mathrm{ER}_{k,\omega_2}}{\mathrm{Max}} \left\| \frac{1}{\left(\mathrm{ER}_{k,\omega_2} - \mu_2\right)} \right\|_2 \tag{64}$$

6. Solution Strategy

After modeling the uncertainties, an MCBD is adapted with ADRO to solve the proposed problem. The flowchart in Figure 3 summarizes the proposed solution. The detailed methodology is explained in the following subsections.

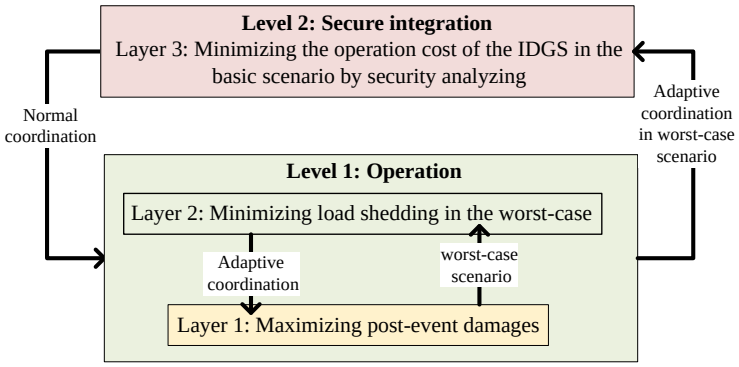

Figure 3. Resilience enhancement of the ADS by making coordination with UGN through the proposed two-level tri-layer ADRO model.

6.1. Modeling Equivalence

To facilitate analysis, the proposed problem can be expressed in a compact form. The following formulation is a simplified version of the tri-layer two-level model for each time interval.

The deterministic mixed-integer nonlinear problem (19) can be formulated as follows

$$C(\mathbf{x},\mathbf{z}) = \underset{\mathbf{x},\mathbf{z}}{\text{Min}}\ \mathbf{c_1}^T\mathbf{x} + \mathbf{c_2}^T\mathbf{z} \tag{65}$$

$$\text{s.t. } \mathbf{A}\mathbf{x} \leq \mathbf{a} \tag{66}$$

$$\mathbf{B}\mathbf{z} \leq \mathbf{b} \tag{67}$$

$$\mathbf{D_1}\mathbf{x} + \mathbf{D_2}\mathbf{z} \leq \mathbf{d}, \tag{68}$$

where **A**, **B**, **D** are matrices of auxiliary coefficients and **a**, **b**, **d** are vectors of auxiliary parameters of the compact model. The objective function (65) is a compact matrix representation of minimizing the cost function *C* in the post-event situation. For notational brevity, **x** and **z** are, respectively, vectors of decision variables to model the energy consumed by ADS (i.e., power and gas) and load shedding. These decision variables are minimized, considering constraints (66)–(68). Constraints (66) and (67) are related to the capacity limitations (10)–(13), (21)–(33), and (35)–(42). The last inequality (68) models constraints (20) and (43).

6.2. Final Model Formulation

The solution method must be adopted to post-event operational requirements for various uncertainties and be able to deal with practical scheduling plans for HILP events. The proposed tri-layer two-level problem can be solved using an adaptive mixed-integer distributionally robust scheduling model considering the uncertainties raised from EC, EZ, and ER. Correspondingly, to model the solution process the following adaptive robust optimization model can be obtained from (65).

$$C(\mathbf{x},\mathbf{z}) = \underset{\mathbf{x},\mathbf{z}}{\text{Min}} \left[\mathbf{c_1}^T\mathbf{x} + \underset{\mathbf{z}|\mathbf{u}}{\text{Max}}\ \underset{\mathbf{z}}{\text{Min}}\ \mathbf{c_2}^T\mathbf{z}\right]. \tag{69}$$

The resilience enhancement factor **z** is closely related to the values of **u**. Hence, the Level 1 solver finds the worst-case operation point of ADS to specify the most robust interconnection with UGN considering various realization distributions. This is achieved by a resilience-oriented max − min function. Then, a robust scheduling of supplied power is achieved by incorporating the energy costs of IDGS at Level 2. The general form of the tri-layer two-level ADRO model is presented as follows for each uncertain probability distribution ω_p constructed from sampled data of ω.

$$C^{(\omega_p)}(\mathbf{x},\mathbf{z}^{(\omega_p)}) = \underset{\mathbf{x},\mathbf{z}}{\text{Min}}[\mathbf{a_1}^T\mathbf{x} + \underset{\pi_1,\ldots,\pi_W \geq 0}{\text{Max}}\ \underset{\boldsymbol{z_{\omega_p}} \in Z^{(\omega_p)}(\mathbf{x},\mathbf{u})}{\text{Min}}\ \sum_{\omega_p=1}^{W} \pi_{\omega_p}\mathbf{a_2}^T\mathbf{z}_{\omega_p}] \quad \forall\omega_p,$$

subject to

$$Z^{(\omega_p)}(\mathbf{x},\mathbf{u}) = \left\{ z_{\omega_p} \left| \begin{array}{c} (66)\text{–}(68) \\ \sum\limits_{\omega_p=1}^{W} \pi_{\omega_p} = 1 \\ \sum\limits_{\omega_p=1}^{W} \left|\pi_{\omega_p} - \hat{\pi}_{\omega_p}\right| \leq (1-\Gamma) \end{array} \right. \right\} \qquad \forall\omega_p, \tag{70}$$

As shown in (70), the resilience factor **z** is not known exactly in advance. Thus, a set of random distributions with different probabilities π is castrated, considering the vector $Z^{(\omega_p)}$. The value of **z** in each distribution depends on the values of **x** and **u**. By identifying the worst-case through the max − min function, the distributionally robust energy scheduling of the proposed IDGS can be achieved. The set of constraints (70) states that the limits of the decision variables must be considered for each distribution of the ADRO problem and that the sum of all probability factors must be equal to 1. Since the proposed stochastic framework has a large sample space, the variation in the probability π_ω of realized distributions with respect to the probability $\hat{\pi}_\omega$ derived from the data is limited to Γ.

The proposed resilience-oriented ADRO problem is a complex two-level tri-layer optimization program shown in Figure 3. The objective function in (70) is different from the compact representation (65) because the ambiguity set of uncertainties are modeled by distributions in the full model. It also differs from (69), because the full model specifies a set of various probabilities for each random distributions. Moreover, while conventional adaptive robust optimization is associated with a single worst-case scenario, ADRO is driven by the statistical characterization of distributions developed at Level 1 of the model. In this way, ADRO (70) can take into account ambiguous variations from the expected values and simultaneously cover both the results obtained by solving (65) and (69).

6.3. The Proposed Methodology

To allow for the solution of the proposed problem using commercial software packages and to mitigate computational issues, we develop a MCBD algorithm considering post-event ω_p. The MCBD approach incorporates multiple cuts into the master problem. A similar method for a stochastic (scenario-based) approach was proposed in [43]. In contrast to [43], this paper generates multiple cuts for each distribution rather than individually for each scenario. Consequently, the master problem acquires more realistic and detailed information, which definitely contributes to a more accurate outcome.

(1) Initialization: The BD algorithm requires a linear sub-problem. The power flow constraint (22) and the Weymouth gas flow (35) cause the problem to become nonlinear. In this paper, both constraints are linearized using an approach similar to [44]. First, the starting points of variables $\bar{\mathbf{x}}$ are calculated using the first-order Taylor expansion. Then, an approximate canonical form is obtained by defining coefficients $\mathbf{H}, \mathbf{h}$ and $\mathbf{M}, \mathbf{m}$. Finally, based on the second-order cone approach, a convex form of the nonlinear constraints is constructed, as shown below.

$$\|\mathbf{Hx}\|_2 \leq \mathbf{hx}, \tag{71}$$

$$\|\mathbf{M_1}(\bar{\mathbf{x}})\mathbf{x} + \mathbf{M_2}(\bar{\mathbf{x}})\|_2 \leq \mathbf{m_1}(\bar{\mathbf{x}})\mathbf{x} + \mathbf{m_2}(\bar{\mathbf{x}}). \tag{72}$$

In addition, at the first iteration, the initial decision variables of Level 1 are set as feasible solutions. These initial values are obtained by solving (65)–(68). The lower and upper bounds are considered as $\pm\infty$. Furthermore, the convergence tolerance for Level 2 is specified by $\epsilon > 0$.

(2) Master Problem: To find the optimal Level 2 decision for the worst-case expected cost, master problem (73) is minimized, under constraints (74)–(77).

$$\underset{\mathbf{x},\mathbf{\Phi}^{(i)}}{\text{Min}}\ \mathbf{c_1}^T\mathbf{x}^i + \sum_{\omega_p=1}^{W} \pi_{\omega_p}\mathbf{\Phi}^{(i)} \qquad \forall\omega_p, \forall i, \tag{73}$$

s.t.

$$A\mathbf{x}^i_{\omega_p} \leq a \qquad \forall\omega_p, \forall i, \tag{74}$$

$$\left(\|\mathbf{Hx}\|_2\right)_{\omega_p} \leq \boldsymbol{hx_{\omega_p}} \qquad \forall\omega_p, \forall i, \tag{75}$$

$$\left(\left\|\boldsymbol{M_1}(\bar{x})\boldsymbol{x_{\omega_p}} + \mathbf{M_2}(\bar{\mathbf{x}})\right\|_2\right)_{\omega_p} \leq \boldsymbol{m_1}(\bar{x})\boldsymbol{x_{\omega_p}} + \mathbf{m_2}(\bar{\mathbf{x}}) \qquad \forall\omega_p, \forall i, \tag{76}$$

$$\mathbf{\Phi}^{(i)}_{\omega_p} \geq \gamma^{(i-1)}[e - E\mathbf{x}^i_{\boldsymbol{\omega_p}}] \qquad \forall\omega_p, \forall i, \tag{77}$$

where $\Phi^{(0)}$ is the set of initialized decision variables and $\Phi^{(i)}$ is an approximation for the cost of Level 1 in the i^{th} iteration. In (73), the results of the master problem determine the lower bound of the proposed ADRO problem for each scenario. Inequalities (74)–(76) indicate the convex formulation (71) and (72) should be applied for each ω_p. For constraint (68), including complicating variable $\mathbf{z}$, dual variable γ is defined in (77) to generate Benders' cuts for each iteration.

(3) Sub-problem: In the proposed MCBD compared to the conventional BD, the sub-problem generates multi cuts to analyze the ADRO problem in more detail. The following model defines the sub problem $SP^{(\omega_p)}$.

$$\underset{\pi_1,\ldots,\pi_W \geq 0}{\text{Max}} \ \underset{\mathbf{z}^i_{\omega_p}}{\text{Min}} \sum_{\omega_p=1}^{W} \pi_{\omega_p} \mathbf{a_2}^T \mathbf{z}^i_{\omega_p} \qquad \forall \omega_p, \forall i, \tag{78}$$

$$\mathbf{z}^i_{\omega_p} \leq e - E\mathbf{x}^{*,i}_{\omega_\mathbf{p}} \qquad \forall \omega_p, \forall i, \qquad : \gamma^{(i)} \tag{79}$$

$$D\mathbf{z}^i_{\omega_p} \leq d \qquad \forall \omega_p, \forall i, \tag{80}$$

To calculate $SP^{(\omega_p)}$, W scenarios of each probability distributions ω_{p1} and ω_{p2} are sampled. Since the nature of ω_{p1} and ω_{p2} are different, to achieve an efficient sampling method, two different approaches that utilized random sampling and cluster sampling were used.Since ω_{p1} is constructed based on the synthetic data, equal chance of being selected is considered for every individual array using simple random sampling. On the other hand, ω_{p2} is based on real historical data depending on extreme weather. Therefore, a cluster sampling method is employed. Firstly, the data sets of s and v are divided into the various clusters (c) modeling the intensity of situations. Then, samples are chosen systematically to ensure representation from each cluster using LHS. The total number of selected sample is W. Finally, the dual sub-problem is degenerated feasible W cuts for the same MP.

The sub-problems are solved in parallel and each sub-problem generates a cut added to the master problem. Indeed, the multiple-cut sub-problem version ($SP^{(\omega_p)}$) of BD is generated from all sampled scenarios, which is different from the single-cut one (SP). By implementing MCBD to solve the ARDO problem, the optimized value (maximum) of (78) among multi-cuts returned to MP in each iteration.

7. Numerical Results

7.1. Case Study and Input Data

The efficiency of the proposed resilience enhancement strategy is demonstrated using the test systems depicted in Figure 4. The network parameters are adopted from [45]. The configuration of wind and solar, and the energy storage capacity have been selected such that the IDGS operates under normal (pre-event) conditions, i.e., with no load shedding. The configuration of wind and solar, and the energy storage capacity have been selected such that the IDGS operates under a pre-event (normal) conditions, i.e., with no load shedding. To properly implement the proposed optimization approach, the test ADS is sectionalized into four distinct zones. These zones include RESs and ESs of various sizes.

Real-world data are used to train the model and calculate the power generated by RESs. The two data sets include 4 years (D = 1462) of hourly values v (at 10 m) and s (at 2 m) collected on the South Campus of the University of Alberta, Edmonton, Canada, from 2018 to 2022. This data is recorded by weather stations operating in the province of Alberta and provided by the Alberta Climate Information Service [46]. These time series are processed using the proposed DLSTM method. Considering the hourly-based DA optimization (T = 24), the raw time series data are distributed among 24 subtasks that operate in parallel. Therefore, the proposed matrix-based prediction method has dimensions of 24 rows and 1462 columns. To achieve more practical results, avoid the need for filtering, and capture rare events, each distributed data set is classified into three clusters using the k-means algorithm. Thus, for each data set, the model is run 72 times to predict three variables in 24 time slots. Finally, as a case study, the predicted v and s data for 15 February 2022 (chosen arbitrarily) is used as the input to calculate the power generated by RESs. Theses predicted values are $\mu_\mathbf{2}$ used to construct matrix ER.

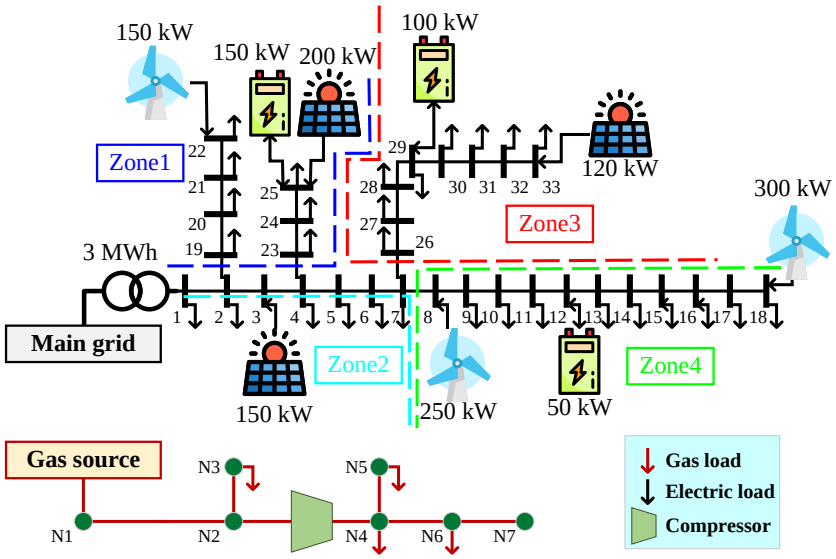

Figure 4. Topology of the modified IEEE 33-bus ADS and seven-node UGN.

The proposed diurnal learning approach is implemented in Python 3.8.15 using package Keras 2.7.0 with TensorFlow 2.7.1 backend. For each hour (subtask), the data is divided into training (75%), validation (15%), and testing (10%) subsets [33]. The DLSTM network layout is identical for all hours using (54)–(59). It is a sequential model with 64 hidden layers including 32 LSTM blocks/neurons with *ReLU* activation function, and a dense output layer. MSE is used as a loss function to optimize the learning rate, epoch size, and time step by Adam optimizer for each hour. The developed software is run on a virtual server with NVIDIA GPU and 32 GB of RAM [47]. Figure 5 shows the generated input data for handling of uncertainties in the post-event situation. Figure 5a depicts DA values of v and s obtained from all subtasks at each hour. This figure includes results of k-means clustering for W = 3 (cf. the three semi-transparent areas of different colors) and DLSTM results (solid lines) for each cluster as μ_2. The weight of each data point is assigned by evaluating the standard deviation and cluster density [48]. Figure 5b presents realization scenarios of CLs' factor at each bus generated by the MC method. Finally, using (44)–(53) and (60)–(64), the results illustrated in Figure 5a,b are utilized to construct ω_{p1} and ω_{p2}, respectively.

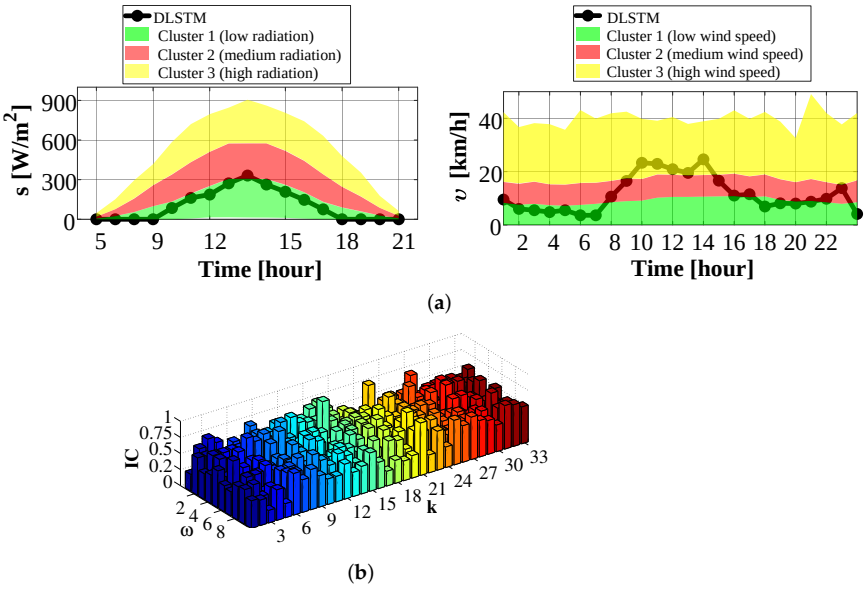

Figure 5. Data preparation (**a**) predicted wind speed and solar radiation by the proposed DLSTM method, (**b**) critical load factors in each bus for 10 scenarios.

7.2. Results and Discussion

After modeling the uncertainties the proposed solution methodology is applied using MCBD. The proposed methodology was simulated using CPLEX solver in GAMS 24.1.2 [49] and executed on a PC with an Intel Core i7, 1.8 GHz CPU, and 8 GB of memory.

(1) Resilience enhancement:

The expected optimal problem-solving outcomes are illustrated for three distinct phases to allow for a detailed comparison. In addition to the pre-event and post-event phases, the base IDGS case (when both the integrated ADS and the UGN are operating normally) is also considered.

To keep the presentations simple, the operation of the ESs is only depicted for the pre-event phase, as shown in Figure 6. To prevent load shedding, the system has been modified so that ADS exchanges power with ESs using their maximum capacities most of the time. Consequently, this system is more vulnerable and should be made resilient against potential outages in any zone.

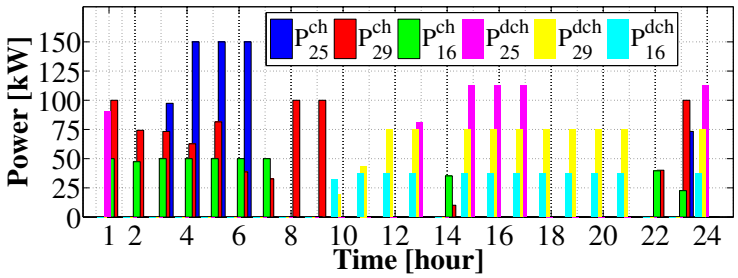

Figure 6. Optimal status of ESs.

By applying the solution in Layer 1, the worst-case scenario includes the outage of lines that disconnect Zone 1 from the system (lines between buses 2–19 and 4–23). Taking this outage into account, Layer 2 recognizes the appropriate buses for the installation of GTs considering the l^{sh} of each bus. This way, buses 19 and 24 are identified as the most vulnerable. Finally, the results of Layer 3 determine the appropriate capacities and gas nodes to coordinate between ADS and UGN so that the resilience of the system is enhanced. This results in nodes N2 and N3 supplying the GTs in buses 19 and 24, with capacities of approximately 750 kW and 800 kW, respectively.

Figures 7 and 8 show the results of the proposed two-level approach for P^{P} and P^{GT}, respectively. As can be seen in Figure 7, the pattern of power received from the upstream grid during normal pre-event operation of ADS follows the price of power, RESs generation, and load profile.

Due to outages, the loads in Zone 1 are supplied by local suppliers. At the same time, the secure power flow constraints of the ADS limit the power received from the upstream feeder. Consequently, during the post-event phase, the DA values of P^{P} are relatively low compared to the pre-event phase.

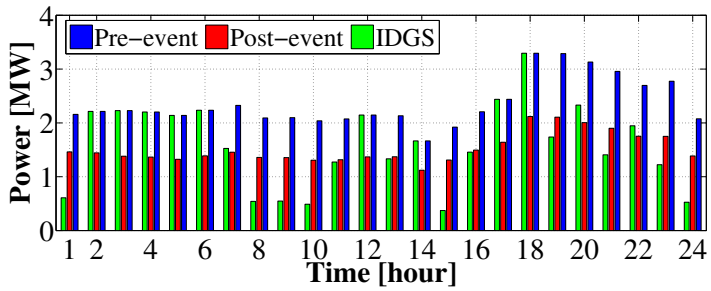

Figure 7. Optimal power received from upstream grid.

To eliminate l^{sh} and enhance the resilience of the ADS, GTs use the pattern of P^{P} which is almost the same as post-event in Figure 8. As shown in the same figure, the installed GTs can be alternatively used as backup suppliers during the normal operation of the IDGS. As a result, for peak load and high power price hours, the operation of GTs is cost-efficient as they consume relatively inexpensive gas from UGN (G^{GT}) to generate power for ADS (P^{GT}).

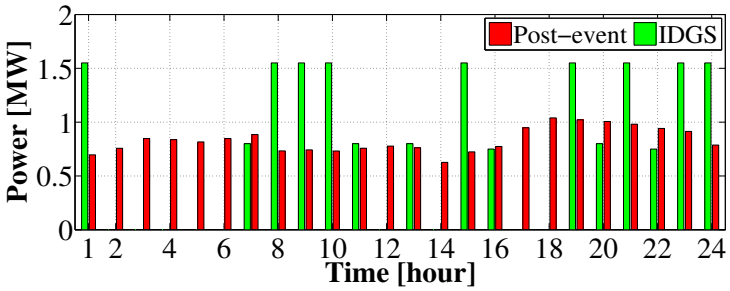

Figure 8. Optimal power generated by GTs.

Although the proposed solution for integrating ADS and UGN is the optimal method for enhancing resilience, it is unlikely that the GT capacity determined this way would be considered in a practical coordination scheme. In practice, additional operational variables, such as the vulnerability of UGN and variation in gas load, should be included in the security analysis. When the GTs are installed, the voltage stress of the ADS buses increases significantly. In addition, the node pressure of the connected GTs drops to the minimum level. The effect of different GT penetration rates on l_{sh}, for the worst-case scenario, is shown in Figure 9. According to the figure, the level of commitment between ADS and UGN operators has a direct impact on the total DA load shedding and resilience of the ADS. However, due to the operational limitations for higher penetration rate of GTs, the amount of critical load shedding is higher than the non-critical load shedding in the proposed decision-making approach. For the IDGS, the best commitment of GT capacity for coordination can be selected using the results shown in Figure 9.

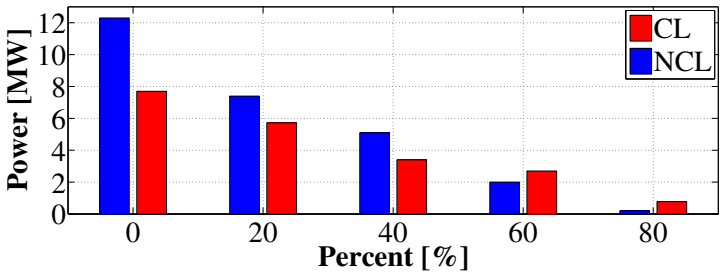

Figure 9. Total day ahead l_{sh} vs. GTs penetration rate considering two types of loads for the worst-case scenario.

The optimization results of the proposed system depend on the degree of uncertainty at Level 1. Table 2 compares the results obtained with two deterministic methods (MILP and MINLP) using a sample scenario, and two robust models (ARO [35] and ADRO) using a set of realization scenarios. It can be seen that linearization (MILP) results in lower l_{sh} compared to the basic nonlinear formulation (MINLP). The remaining two robust scenario-based models demonstrate the effect of various uncertainty parameters on resilience metric calculations. When uncertainties are incorporated into both optimization methods (ARO and ADRO), the value of l_{sh} increases. However, the results of the ADRO approach are more realistic and practical than those of ARO for different levels of uncertainties. In other words, in ARO, for different uncertainty budget percentages (Γ^{*}), the operation costs of Level 1 are higher than for the corresponding percentages Γ in ARDO. Indeed, the ARO method constructs a deterministic calculation based on the most likely realization scenario as the

worst-case. In contrast, the proposed ADRO method considers the occurrence probabilities, or the symmetry in the uncertainty distributions. As a consequence, considering the uncertainty distribution results in a smaller gap between the real-time and DA analyses.

Table 2. Resilience comparison of different optimization methods during post-event for Level 1.

MINLP					**MILP**				
l^{sh}(MW)	18.21				l^{sh}(MW)	17.51			
ARO [35]					ADRO				
Γ^*(%)	95	90	85	80	Γ(%)	95	90	85	80
l^{sh}(MW)	22.19	22.85	23.91	24.89	l^{sh}(MW)	19.80	20.01	20.78	21.23

(2) Learning method:

Figure 10a and Figure 10b depict, respectively, the results of the DA forecasts for the wind speed and solar irradiance test sets. For a fair comparison, the parameters for LSTM and DLSTM neural networks are identical. The results shown in the figures confirm that the new forecasting model can predict both variables effectively and with high accuracy. This is due to the fact that the DLSTM network can decrease the sample variation by extracting the hourly features leading to bias reduction.

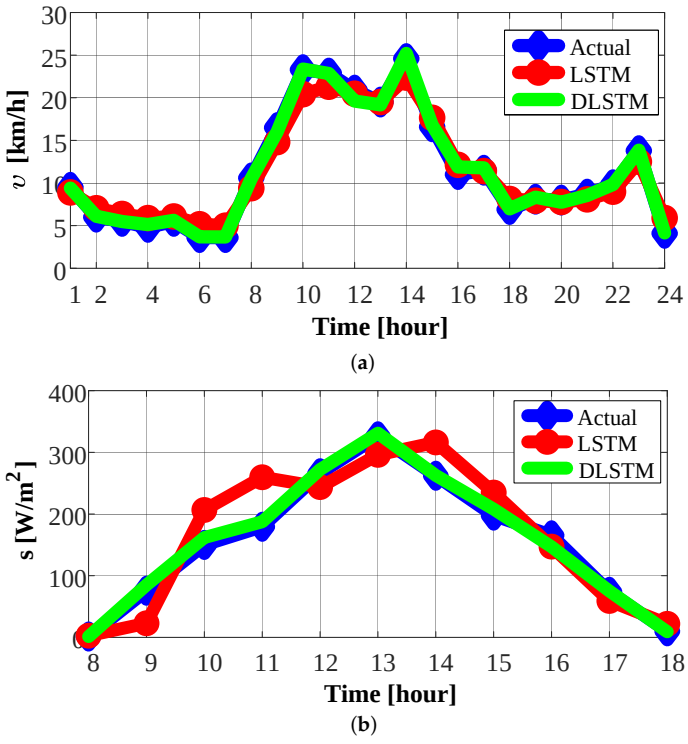

Figure 10. Comparison results of the proposed DLSTM for 15 February 2022. (**a**) wind speed, (**b**) solar radiation.

Prediction accuracy is also evaluated using two commonly used error metrics: MAE and MAPE. Forecast errors are listed in Table 3. Using DLSTM, the MAE and RMSE for v are reduced by about 47% and 71%, respectively, compared to the standard LSTM. For s, the reductions are 76% and 77% for MAE and RMSE, respectively. This confirms that the proposed DLSTM neural network can capture deep generalizations of various time-series data by distributing them across several forecasting tasks. Thus, neither normalization nor filtering is required because the data for each subtask are within its own logical range. This allows DLSTM to generate accurate forecasts for complex time series.

Table 3. Prediction error of conventional LSTM and proposed DLSTM.

Forecasting Method	Wind Speed		Solar Radiation	
	RMSE (km/h)	MAE (km/h)	RMSE (W/m^2)	MAE (W/m^2)
LSTM	3.22	2.34	45.87	30.14
DLSTM	1.71	0.68	11.13	6.92

The illustrations in Figure 11, which demonstrate the error frequency of 24 subtasks, confirm the results presented in Table 3. According to the entire data set of v, the RMSE and MAE values for the subtasks are improved between the ranges of $[34\%, 52\%]$ and $[67\%, 77\%]$. Similarly, each subtask of the s data set achieves RMSE and MAE improvement ranges of $[34\%, 93\%]$ and $[57\%, 95\%]$, respectively. As indicated previously, to ensure a fair comparison, the fitting model for both the LSTM and DLSTM approaches is the same. However, the values in Figure 11 can be further improved by optimizing the hyperparameters of the neural network in each subtask.

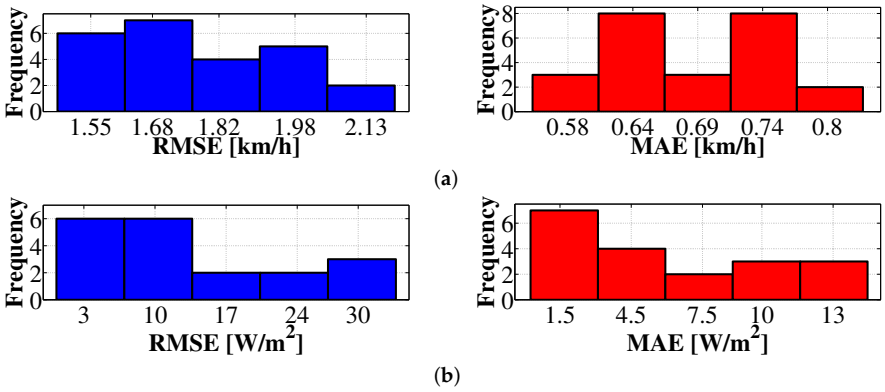

Figure 11. Error distributions of subtasks: (**a**) Wind speed, (**b**) solar radiation.

8. Conclusions

This article proposes a two-level tri-layer problem to improve the resilience of ADS by coupling it with UGN. The complex resilience-oriented problem is solved using an ADRO approach based on the MCBD method. Compared to ARO, the proposed approach results in approximately 11% and 15% reduction in load shedding for higher and lower uncertainty budget percentages, respectively. To handle the uncertainty of the post-event structural consequences, realization scenarios are modeled using the MC method. The results confirm that the use of GTs with optimal capacity and location enhances the resilience of the system against HILP events. Accordingly, optimizing the location and capacity for coordination between ADS and UGN can reduce load shedding by approximately 94% compared to uncoordinated systems. In summary, the most effective solution for the proposed resilience enhancement approach is a learning-based optimization method for IDGS. An additional contribution is the newly proposed diurnal learning method to address the uncertainties of weather-related power generated from RESs. This method, DLSTM, achieves more accurate and practical results than conventional LSTM. In future work, we plan to extend the proposed solution to cover additional resilience enhancement mechanisms such as demand response and electric vehicles.

The proposed approach has several limitations which offer opportunities for its further development. First, it may be possible to develop a more streamlined version of the model that balances the complexity of the resilience-oriented model with computational efficiency. The model also relies on accurate data to effectively capture uncertainties. In scenarios where adequate data are not available, the performance of the model may be compromised, leading to suboptimal resilience outcomes. In addition, the presented study focuses mainly

on the technical aspects of enhancing power system resilience, not considering social and economic aspects such as costs, the regulatory environment, and public acceptance. These considerations are critical for the real-world adoption of the proposed resilience enhancement solutions and can be addressed in future work.

Supplementary Materials: The following supporting information can be downloaded at: https://www.mdpi.com/article/10.3390/en17246270/s1.

Author Contributions: Conceptualization, B.F. and P.M.; methodology, B.F. and P.M.; investigation, B.F.; resources, P.M.; writing—original draft preparation, B.F.; writing—review and editing, P.M.; supervision, P.M.; project administration, P.M.; funding acquisition, P.M. All authors have read and agreed to the published version of the manuscript.

Funding: This research has been supported by the Natural Sciences and Engineering Research Council (NSERC) of Canada grant (award number 2024-04565), and by the U.S.-Canada Center on Climate-Resilient Western Interconnected Grid (NSF WIRED Global Center) funded jointly by the National Science Foundation (award number 2330582) and NSERC (award number 2023-585094).

Data Availability Statement: Data are available on request due to restrictions (large data size). Minimal data representing the original were provided at submission and are available in supplementary file.

Conflicts of Interest: The authors declare no conflict of interest.

Nomenclature

HILP	High-impact low-probability
CL	Critical load
NCL	Non-critical load
UGN	Urban gas network
RES	Renewable energy source
ADS	Active distribution system
GT	Gas turbine
ESS	Energy storage system
IDGS	Integrated distribution and gas system
MILP	Mixed integer linear programming
DLSTM	Diurnal long short-term memory
ADRO	Adaptive distributionally robust optimization
WT	Wind turbines
PV	Photovoltaic panels
DA	Day ahead
MAE	Mean absolute error
MAPE	Mean absolute percentage error
MC	Monte-Carlo
C_{mn}	Waymouth constant
p_{mn}	Node pressure of natural gas network [bar]
$\tilde{q}(t)/q_{mn,t}$	Average/Transmitted Gas flow in pipeline [Mm^3]
LP	Line-pack between nodes [kcf]
α	Gas to power conversion factor [kW/kcf]
RU^{GT}/RD^{GT}	Ramp-up/Ramp-down rate of GT [kW]
ω	ambiguity set
$\omega_1/\ \omega_2$	Sample scenarios of EC/ ER
EC	Encoding matrix of CLs
$\mathcal{M}$	Momentum-based ambiguity set
ER	Encoding matrix of generated power from RESs
π	Probability factor
$\mathcal{S}$	Support
μ	Mean
$\mathbf{\Sigma}$	Covariance

ς_1/ς_2	Controller of ambiguity set
f	Forgetting gate output
h	Hidden layer output
w	Connection weight
ω_p	Probability distributions
ϵ	Convergence tolerance of MCBD
W	Total probability distributions
d	Daily time intervals
i	Iteration of MCBD
C^{P}	Power price [USD/kw]
$(.)^{0/1}$	Pre-/Post-event notation
$P^{\mathrm{P}}/Q^{\mathrm{P}}$	Active/reactive power received from upstream grid [kW]
t	Time [h]
T	Total operation time [24 h]
D	Total day interval of data set
$K/N/C/Z$	Total bus/node/coordination point/zone
$P^{ch/dch}$	ESS's charging/discharging power [kW]
I_{kj}	Squared current magnitude from k to j [A]
U_k/U_j	Squared voltage magnitude of bus k/j [V]
r/x	resistance/inductance [Ω]
$v_{ci}/\ v_{co}/\ v_r$	Cut-in/ cut-out/ rated wind speed [m/s]
s_r	Rated solar radiation [W/m^2]
s	Solar radiation [W/m^2]
v	Wind speed [m/s]
$(.)^{\max/\min}$	Maximum/minimum limitation
E	State of energy [kWh]
$I^{ch/dch}$	ESS's charging/discharging status [binary]
η	Efficiency of ESS [%]
C^G	Natural gas price [USD/kcf]
G^{GT}	Consumed natural gas by GTs [kcf]
ρ	Penalty of load shedding [USD/kW]
W_1/W_2	Total scenario number of EC and ER
β	Depth of discharge [%]
$l^{\mathrm{sh\|cl}}/l^{\mathrm{sh\|ncl}}$	Load shedding of CL/NCL [kW]

References

1. Abdin, I.; Fang, Y.P.; Zio, E. A modeling and optimization framework for power systems design with operational flexibility and resilience against extreme heat waves and drought events. *Renew. Sustain. Energy Rev.* **2019**, *112*, 706–719. [CrossRef]
2. Ravadanegh, S.N.; Jamali, S.; Vaniar, A.M. Multi-infrastructure energy systems resiliency assessment in the presence of multi-hazards disasters. *Sustain. Cities Soc.* **2022**, *79*, 103687. [CrossRef]
3. Darvish, S.M.; Derakhshan, G.; Hakimi, S.M. Enhancing resilience of the smart urban electrical and gas grids considering reserve scheduling and pre-event responses via the onsite supply strategy of the energy storage systems and demand response. *J. Energy Storage* **2024**, *83*, 110633. [CrossRef]
4. Jia, K.; Liu, C.; Li, S.; Jiang, D. Modeling and optimization of a hybrid renewable energy system integrated with gas turbine and energy storage. *Energy Convers. Manag.* **2023**, *279*, 116763. [CrossRef]
5. Manesh, M.K.; Firouzi, P.; Kabiri, S.; Blanco-Marigorta, A.M. Evaluation of power and freshwater production based on integrated gas turbine, S-CO2, and ORC cycles with RO desalination unit. *Energy Convers. Manag.* **2021**, *228*, 113607. [CrossRef]
6. Sayed, A.R.; Wang, C.; Bi, T. Resilient operational strategies for power systems considering the interactions with natural gas systems. *Appl. Energy* **2019**, *241*, 548–566. [CrossRef]
7. Kwasinski, A. Technology planning for electric power supply in critical events considering a bulk grid, backup power plants, and micro-grids. *IEEE Syst. J.* **2010**, *4*, 167–178. [CrossRef]
8. Ahmed, Z.; Nasir, M.; Alsekait, D.M.; Shah, M.Z.H.; AbdElminaam, D.S.; Ahmad, F. Control Conditions for Equal Power Sharing in Multi-Area Power Systems for Resilience Against False Data Injection Attacks. *Energies* **2024**, *17*, 5757. [CrossRef]
9. Xu, N.; Guikema, S.D.; Davidson, R.A.; Nozick, L.K.; Çağnan, Z.; Vaziri, K. Optimizing scheduling of post-earthquake electric power restoration tasks. *Earthq. Eng. Struct. Dyn.* **2007**, *36*, 265–284. [CrossRef]
10. Trakas, D.N.; Hatziargyriou, N.D. Optimal distribution system operation for enhancing resilience against wildfires. *IEEE Trans. Power Syst.* **2017**, *33*, 2260–2271. [CrossRef]

11. Sharma, A.; Srinivasan, D.; Trivedi, A. A decentralized multi-agent approach for service restoration in uncertain environment. *IEEE Trans. Smart Grid* **2016**, *9*, 3394–3405. [CrossRef]
12. Wang, Z.; Wang, J.; Chen, C. A three-phase microgrid restoration model considering unbalanced operation of distributed generation. *IEEE Trans. Smart Grid* **2016**, *9*, 3594–3604. [CrossRef]
13. Xu, G.; Guo, Z. Resilience enhancement of distribution networks based on demand response under extreme scenarios. *IET Renew. Power Gener.* **2024**, *18*, 48–59. [CrossRef]
14. Wang, Y.; Xu, Y.; He, J.; Liu, C.C.; Schneider, K.P.; Hong, M.; Ton, D.T. Coordinating multiple sources for service restoration to enhance resilience of distribution systems. *IEEE Trans. Smart Grid* **2019**, *10*, 5781–5793. [CrossRef]
15. Samani, E.; Aminifar, F. Tri-level robust investment planning of DERs in distribution networks with AC constraints. *IEEE Trans. Power Syst.* **2019**, *34*, 3749–3757. [CrossRef]
16. Hussain, A.; Musilek, P. Resilience Enhancement Strategies For and Through Electric Vehicles. *Sustain. Cities Soc.* **2022**, *80*, 103788. [CrossRef]
17. Faridpak, B.; Farrokhifar, M.; Murzakhanov, I.; Safari, A. A series multi-step approach for operation Co-optimization of integrated power and natural gas systems. *Energy* **2020**, *204*, 117897. [CrossRef]
18. Faridpak, B.; Farrokhifar, M.; Alahyari, A.; Marzband, M. A mixed epistemic-aleatory stochastic framework for the optimal operation of hybrid fuel stations. *IEEE Trans. Veh. Technol.* **2021**, *70*, 9764–9774. [CrossRef]
19. Faridpak, B.; Alahyari, A.; Farrokhifar, M.; Momeni, H. Toward Small Scale Renewable Energy Hub-Based Hybrid Fuel Stations: Appraising Structure and Scheduling. *IEEE Trans. Transp. Electrif.* **2020**, *6*, 267–277. [CrossRef]
20. Raheli, E.; Wu, Q.; Zhang, M.; Wen, C. Optimal coordinated operation of integrated natural gas and electric power systems: A review of modeling and solution methods. *Renew. Sustain. Energy Rev.* **2021**, *145*, 111134. [CrossRef]
21. Saravi, V.S.; Kalantar, M.; Anvari-Moghaddam, A. A cooperative resilience-oriented planning framework for integrated distribution energy systems and multi-carrier energy microgrids considering energy trading. *Sustain. Cities Soc.* **2024**, *100*, 105039. [CrossRef]
22. Cong, H.; He, Y.; Wang, X.; Jiang, C. Robust optimization for improving resilience of integrated energy systems with electricity and natural gas infrastructures. *J. Mod. Power Syst. Clean Energy* **2018**, *6*, 1066–1078. [CrossRef]
23. Manshadi, S.D.; Khodayar, M.E. Resilient operation of multiple energy carrier microgrids. *IEEE Trans. Smart Grid* **2015**, *6*, 2283–2292. [CrossRef]
24. Correa-Posada, C.M.; Sánchez-Martın, P. Security-constrained optimal power and natural-gas flow. *IEEE Trans. Power Syst.* **2014**, *29*, 1780–1787. [CrossRef]
25. Wang, C.; Wei, W.; Wang, J.; Liu, F.; Qiu, F.; Correa-Posada, C.M.; Mei, S. Robust defense strategy for gas–electric systems against malicious attacks. *IEEE Trans. Power Syst.* **2016**, *32*, 2953–2965. [CrossRef]
26. Sawas, A.M.; Khani, H.; Farag, H.E. On the resiliency of power and gas integration resources against cyber attacks. *IEEE Trans. Ind. Inform.* **2020**, *17*, 3099–3110. [CrossRef]
27. Kor, Y.; Reformat, M.Z.; Musilek, P. Predicting weather-related power outages in distribution grid. In Proceedings of the 2020 IEEE Power & Energy Society General Meeting (PESGM), IEEE, Montreal, QC, Canada, 2–6 August 2020; pp. 1–5.
28. Shoaei, M.; Noorollahi, Y.; Hajinezhad, A.; Moosavian, S.F. A review of the applications of artificial intelligence in renewable energy systems: An approach-based study. *Energy Convers. Manag.* **2024**, *306*, 118207. [CrossRef]
29. Li, Q.; Zhao, Y.; Yu, F. A novel multichannel long short-term memory method with time series for soil temperature modeling. *IEEE Access* **2020**, *8*, 182026–182043. [CrossRef]
30. Abdel-Nasser, M.; Mahmoud, K.; Lehtonen, M. Reliable solar irradiance forecasting approach based on choquet integral and deep LSTMs. *IEEE Trans. Ind. Informatics* **2020**, *17*, 1873–1881. [CrossRef]
31. Wang, Y.; Shen, Y.; Mao, S.; Chen, X.; Zou, H. LASSO and LSTM integrated temporal model for short-term solar intensity forecasting. *IEEE Internet Things J.* **2018**, *6*, 2933–2944. [CrossRef]
32. Zhou, H.; Zhang, Y.; Yang, L.; Liu, Q.; Yan, K.; Du, Y. Short-term photovoltaic power forecasting based on long short term memory neural network and attention mechanism. *IEEE Access* **2019**, *7*, 78063–78074. [CrossRef]
33. Dolatabadi, A.; Abdeltawab, H.; Mohamed, Y.A.R.I. Deep Spatial-Temporal 2-D CNN-BLSTM Model for Ultrashort-Term LiDAR-Assisted Wind Turbine's Power and Fatigue Load Forecasting. *IEEE Trans. Ind. Informatics* **2021**, *18*, 2342–2353. [CrossRef]
34. Li, M.; Zhang, Z.; Ji, T.; Wu, Q. Ultra-short term wind speed prediction using mathematical morphology decomposition and long short-term memory. *CSEE J. Power Energy Syst.* **2020**, *6*, 890–900.
35. Gholami, A.; Shekari, T.; Grijalva, S. Proactive management of microgrids for resiliency enhancement: An adaptive robust approach. *IEEE Trans. Sustain. Energy* **2017**, *10*, 470–480. [CrossRef]
36. Shao, C.; Shahidehpour, M.; Wang, X.; Wang, X.; Wang, B. Integrated planning of electricity and natural gas transportation systems for enhancing the power grid resilience. *IEEE Trans. Power Syst.* **2017**, *32*, 4418–4429. [CrossRef]
37. Yan, M.; He, Y.; Shahidehpour, M.; Ai, X.; Li, Z.; Wen, J. Coordinated regional-district operation of integrated energy systems for resilience enhancement in natural disasters. *IEEE Trans. Smart Grid* **2018**, *10*, 4881–4892. [CrossRef]
38. Sekhavatmanesh, H.; Cherkaoui, R. A novel decomposition solution approach for the restoration problem in distribution networks. *IEEE Trans. Power Syst.* **2020**, *35*, 3810–3824. [CrossRef]
39. Jiang, J.; Peng, S. Mathematical programs with distributionally robust chance constraints: Statistical robustness, discretization and reformulation. *Eur. J. Oper. Res.* **2024**, *313*, 616–627. [CrossRef]

40. Luo, Z.; Yin, Y.; Wang, D.; Cheng, T.; Wu, C.C. Wasserstein distributionally robust chance-constrained program with moment information. *Comput. Oper. Res.* **2023**, *152*, 106150. [CrossRef]
41. Korstanje, J. *Advanced Forecasting with Pyton*; Apress: Berkeley, CA, USA, 2021.
42. Ren, L.; Dong, J.; Wang, X.; Meng, Z.; Zhao, L.; Deen, M.J. A data-driven auto-CNN-LSTM prediction model for lithium-ion battery remaining useful life. *IEEE Trans. Ind. Informatics* **2020**, *17*, 3478–3487. [CrossRef]
43. Ge, X.; Jin, Y.; Fu, Y.; Ma, Y.; Xia, S. Multiple-cut benders decomposition for Wind-Hydro-Thermal optimal scheduling with quantifying various types of reserves. *IEEE Trans. Sustain. Energy* **2019**, *11*, 1358–1369. [CrossRef]
44. Sayed, A.R.; Wang, C.; Zhao, J.; Bi, T. Distribution-level robust energy management of power systems considering bidirectional interactions with gas systems. *IEEE Trans. Smart Grid* **2019**, *11*, 2092–2105. [CrossRef]
45. Khani, H.; Farag, H.E.Z. Optimal day-ahead scheduling of power-to-gas energy storage and gas load management in wholesale electricity and gas markets. *IEEE Trans. Sustain. Energy* **2017**, *9*, 940–951. [CrossRef]
46. Alberta Climate Information Service (ACIS), Current and Historical Alberta Weather Station Data Viewer, Government of Alberta. 2022. Available online: https://acis.alberta.ca/ (accessed on 13 May 2022).
47. ISAIC: Industry Sandbox for AI Computing, 2022. Available online: https://www.isaic.ca/ (accessed on 11 June 2022).
48. Sagi, O.; Rokach, L. Ensemble learning: A survey. *Wiley Interdiscip. Rev. Data Min. Knowl. Discov.* **2018**, *8*, e1249. [CrossRef]
49. Bussieck, M.R.; Meeraus, A. General Algebraic Modeling System (GAMS). In *Modeling Languages in Mathematical Optimization*; Kallrath, J., Ed.; Springer: Boston, MA, USA, 2004; pp. 137–157. [CrossRef]